Journal of Materials Chemistry B

PAPER

View Article Online
View Journal | View Issue

Cite this: J. Mater. Chem. B, 2014, 2, 1009

Glucose-, pH- and thermo-responsive nanogels crosslinked by functional superparamagnetic maghemite nanoparticles as innovative drug delivery systems†

Ji Liu,[ac] Christophe Detrembleur,*[a] Antoine Debuigne,[a] Marie-Claire De Pauw-Gillet,[b] Stéphane Mornet,[c] Luce Vander Elst,[d] Sophie Laurent,[d] Etienne Duguet*[c] and Christine Jérôme*[a]

Received 16th September 2013
Accepted 26th November 2013

DOI: 10.1039/c3tb21272f

www.rsc.org/MaterialsB

Reversibly crosslinked (RCL) nanogels made of thermo-responsive poly(vinyl alcohol)-*b*-poly(*N*-vinylcaprolactam) copolymers were combined with maghemite nanoparticles and developed as new drug delivery systems (DDS). The crosslinking was formed *via* boronate/diol bonding from the surface-functionalized superparamagnetic maghemite nanoparticles, endowing the DDS with thermo-, pH- and glucose-responsiveness. The capability to load a hydrophobic drug model Nile red (NR) within the RCL nanogels was evaluated, and stimuli-triggered drug release behaviours under different conditions were tested. Zero premature release behaviour was detected at physiological pH in the absence of glucose, whereas triggered release was observed upon exposure to acidic pH (5.0) and/or in the presence of glucose. In light of the superparamagnetic properties of the maghemite nanoparticles and RCL nanogels, magnetically-induced heating, MR imaging performance, as well as remotely magnetically-triggered drug release under alternating magnetic field (AMF), were investigated. Cytotoxicity against fibroblast-like L929 and human melanoma MEL-5 cell lines was assessed *via* the MTS assay. *In vitro* stimuli-triggered release of tamoxifen, a chemotherapeutic drug, was also studied within MEL-5 cell cultures under different conditions. These innovative RCL nanogels, integrating different stimuli-responsive components, hydrophobic chemotherapeutic moieties and also diagnostic agents together *via* reversible crosslinking, are promising new theranostic platforms.

1. Introduction

Stimuli-responsive nano-scale vehicles are gaining increasing attention in the field of drug delivery systems (DDS), since they are able to remain intact within the vasculature for a relatively long period. Such carriers can thus accumulate in some specific sites, such as tumours, *via* the enhanced permeation and retention (EPR) effect, which might maximize their performance in targeted drug delivery, biomedical imaging, gene transfection, chemotherapy, phototherapy, hyperthermia treatment, *etc.*[1,2] Moreover, stimuli-triggered release could be accomplished by taking advantage of their inherent physico-chemical changes in response to some specific external stimuli, such as variation in pH,[3,4] temperature,[5,6] reductive agents[7,8] or glucose concentration,[9,10] and also some external stimuli, such as application of light[11,12] or magnetic field,[3,6] to cite a few. Such kinds of stimuli can be present in some disease microenvironments or introduced manually during the treatments.[13–15] Among these nano-scale vehicles, stimuli-responsive polymer assemblies, *e.g.* micelles, hydrogels, *etc.*, are extensively studied, due to their facile fabrication, high cargo loading capability, controllable release behaviours, *etc.*[14] The major challenge to the application of physically-assembled micelles as DDS *in vivo* should be their poor colloidal and serum stability, which might result in unexpected leaking during the delivery routine and

[a]*Center for Education and Research on Macromolecules (CERM), Department of Chemistry, University of Liège, B6a Sart Tilman, B-4000 Liège, Belgium. E-mail: christophe.detrembleur@ulg.ac.be; c.jerome@ulg.ac.be; Fax: +(32)4-36663497; Tel: +(32)4-3663565*

[b]*Laboratory of Mammalian Cell Culture (GIGA-R), University of Liège, B6c Sart Tilman, B-4000 Liège, Belgium*

[c]*CNRS, Univ. Bordeaux, ICMCB, UPR 9048, F-33600 Pessac, France. E-mail: duguet@icmcb.u-bordeaux1.fr; Fax: +33 540 002 761; Tel: +33 540 002 651*

[d]*Department of General, Organic & Biomedical Chemistry, NMR & Molecular Imaging Laboratory, University of Mons, Avenue Maistriau, 19, B-7000 Mons, Belgium*

† Electronic supplementary information (ESI) available: ^{1}H NMR spectra of the PVAc-*b*-PNVCL and PVOH-*b*-PNVCL copolymers, SEC trace of the PVOH-*b*-PNVCL copolymer, XPS and TGA patterns of the γ-Fe_2O_3 NPs, pictures of the NR-loaded or non-loaded RCL nanogels dispersions, SEM images of the RCL nanogels, TEM images of the RCL nanogels after different treatments, cell viability of the MEL-5 cells after treatment with tamoxifen, or incubation at pH of 7.4 or 5.0 with/without glucose at different concentrations, *etc.* See DOI: 10.1039/c3tb21272f

extremely low delivery efficiency through intravenous injection.[16] An ideal DDS based on polymer assemblies should satisfy the conflicting requirements of (i) high stability in extracellular fluid, so that the vehicles maintain their integrity during the *in vivo* circulation, and (ii) rapid dissociation of the structures upon activation of some specific stimuli, leading to release of the therapeutic agents.[17] As reported, nano-scale polymer assemblies possessing both stimuli-responsiveness and reversibly-crosslinked nanostructures, such as the redox-sensitive bonding,[7,8,18,19] light-sensitive bonding,[20,21] *etc.*, to cite a few, can meet these requirements.

Among those reversible crosslinking strategies, the boronate/diol crosslinking is attracting more interest. Until now, it has been reported to crosslink polymer micelles,[9,22–24] hydrogels,[25–27] or macromolecular stars,[28] reversibly switch on/off the mesoporous silica cavities with boronate-functionalized gold nanoparticles,[29,30] *etc.* The boronate/diol crosslinked micelles or hydrogels are attractive DDS candidates for glucose- or pH-triggered release. The underlying mechanism is based on the fact that, boronate derivatives show high affinity to molecules bearing *cis*-diol groups, and the resultant boronate/diol bonding exhibits sharp responsiveness to variation in pH and/or presence of competing low-molecular-weight diols.[25,26,31] This kind of DDS is of special interest for the treatment of some diseases, such as diabetes,[23–27,29,30,32–36] and also as biosensor devices to monitor the glucose concentrations in the body fluid.[25,31,37–39] However, due to the difference between physiological pH of 7.4 and pK_a of those commonly-used boronate derivatives, such as phenylboronic acid (PBA, pK_a of 8.8) and 3-aminophenylboronic acid (APBA, pK_a of 8.75), it is very difficult to obtain stable crosslinked structures under physiological conditions (pH 7.4). Fortunately, substitutions with some electron-withdrawing groups on the phenyl-ring of PBA molecules could effectively lower the pK_a, which in turn favours the formation of stable boronate/diol bonding under neutral or even weak acidic conditions.[40] As reported by Basu and colleagues,[41] the substitutions, on the phenyl-ring, with carboxy- and nitro-groups could effectively decrease the pK_a value from 8.8 (PBA) to *ca.* 6.0 (3-carboxy-5-nitrophenylboronic acid, CNPBA), suggesting a stable crosslinked structure under physiological pH (7.4), once CNPBA moieties were used for crosslinking.

Herein, thermo-induced polymer micelles of poly(vinyl alcohol)-*b*-poly(*N*-vinylcaprolactam) (PVOH-*b*-PNVCL) were formed above the lower critical solution temperature (LCST) of PNVCL blocks. Then maghemite nanoparticles (γ-Fe_2O_3 NPs) functionalized with CNPBA moieties (Scheme 1-1) were used to reversibly crosslink (RCL) the PVOH corona *via* boronate/diol bonding. Finally, reversibly crosslinked (RCL) nanogels were obtained upon cooling the suspension below the LCST (Scheme 1-2). These RCL nanogels are expected to accomplish a zero premature release during the *in vivo* circulation; nevertheless, triggered release could be achieved upon some stimuli, such as variation in pH and/or presence of competing low-molecular-weight diols, such as glucose. Furthermore, due to the superparamagnetic properties of the γ-Fe_2O_3 NPs, these RCL nanogels could also be developed for magnetically-guided delivery, MR imaging, magnetically-triggered drug release, *etc.*

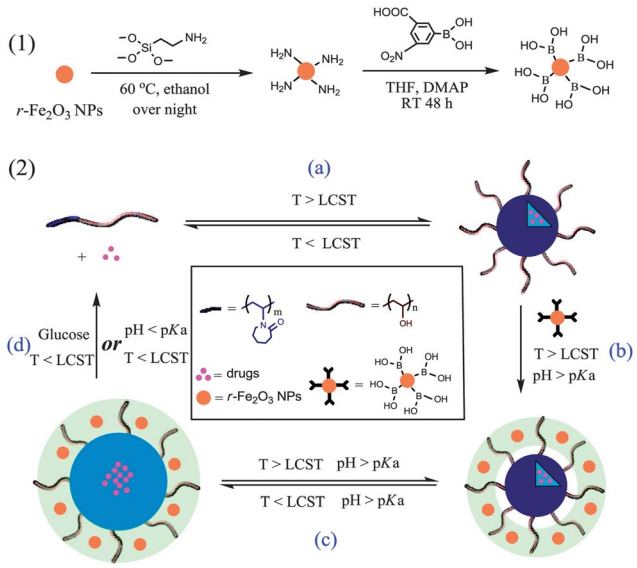

Scheme 1 Surface functionalization of the γ-Fe_2O_3 NPs with boronic acid derivatives: 3-carboxy-5-nitrophenylboronic acid (1); thermally-induced micelle formation and hydrophobic drug loading of the PNVCL core above the LCST (2-a); crosslinking of the PVOH corona of the micelles with the γ-Fe_2O_3 NPs functionalized with the boronic acid derivative (2-b); formation of drug-loaded RCL nanogels after cooling down below the LCST (2-c) and glucose- and pH-triggered release of the drug molecules (2-d).

2. Experimental

2.1 Materials

(3-Aminopropyl)triethoxysilane (APTES, 97%), Nile red (NR, 95%), (4-dimethylamino)pyridine (DMAP, 99%), 3-carboxy-5-nitrophenylboronic acid (CNPBA, 99%), iron(III) chloride hexahydrate ($FeCl_3 \cdot 6H_2O$, 97%), iron(II) chloride tetrahydrate ($FeCl_2 \cdot 4H_2O$, 98%), hydrogen chloride (HCl, 37%), iron(III) nitrate nonahydrate ($Fe(NO_3)_3 \cdot 9H_2O$, 98%), ammonia hydroxide solution ($NH_3 \cdot H_2O$, 28–30%), nitric acid (HNO_3, 70%), sodium phosphate dibasic (Na_2HPO_4, 98.5%), potassium phosphate monobasic (KH_2PO_4, 98%) and sodium hydroxide (NaOH, 99%) were purchased from Aldrich. 3-(4,5-Dimethylthiazol-2-yl)-5-(3-carboxymethoxyphenyl)-2-(4-sulfophenyl)-2H-tetrazolium (MTS) was purchased from Promega (Madison, USA). DMEM medium (low glucose, without sodium pyruvate), L-glutamine, phosphate buffered saline (PBS, without Ca^{2+} and Mg^{2+}), fetal bovine serum (FBS) and trypsin were obtained from Biowhittaker (Walkersville, MD). PBS buffer solutions (with Ca^{2+} and Mg^{2+}), penicillin G, streptomycin and trypsin–EDTA (0.5/0.2 vol.%, ×10) were purchased from GIBCO BRL (Gaithersburg, MD). Vinyl acetate (VAc, 99%, Acros) was dried over calcium hydride, degassed by several freeze–thawing cycles before distillation under reduced pressure and stored under argon. 2,2,6,6-Tetramethylpiperidine-1-oxy (TEMPO, 98%, Aldrich) was stored at +6 °C and used as received. Bis(acetylacetonato)-cobalt(II) ($Co(acac)_2$, 98%, Acros) was used as received and stored under argon. 2,2′-Azobis(4-methoxy-2,4-dimethyl valeronitrile) (V-70, 96%, Wako) was stored at −20 °C and used as received. *N*-Vinylcaprolactam (NVCL, 98%, Aldrich)

monomers were dissolved in dry dimethylformamide (NVCL/DMF = 1/1 w/v%), degassed by 30 min argon bubbling and then dried with molecular sieves.

2.2 Methods

Synthesis of poly(vinyl alcohol)-*b*-poly(*N*-vinylcaprolactam) (PVOH-*b*-PNVCL) copolymers. PVOH-*b*-PNVCL copolymers were obtained by hydrolysis of poly(vinyl acetate)-*b*-poly(*N*-vinylcaprolactam) copolymers (PVAc-*b*-PNVCL), prepared by cobalt-mediated radical polymerization (CMRP)[42,43] according to a previously reported procedure.[44] Typically, the alkylcobalt(III) adduct (0.186 mmol) in CH_2Cl_2, prepared from a previously reported protocol,[45] was taken in a 100 mL round-bottom flask and the solvent was eliminated under reduced pressure. Vinyl acetate (6.65 mL, 0.072 mol) was then added with a syringe under argon and the purple mixture was stirred at 40 °C for 6 h, with a monomer conversion of *ca.* 46.6%. After elimination of the residual monomer under reduced pressure, the pink PVAc–Co macroinitiator was obtained ($M_{n,SEC,THF} = 1.20 \times 10^4$ g mol^{-1}, $M_w/M_n = 1.05$; $M_{n,SEC,DMF} = 4.42 \times 10^4$ g mol^{-1}, $M_w/M_n = 1.04$) and stored under an inert atmosphere. After cooling down to 0 °C, NVCL (10.4 g, 75 mmol) solution in DMF (10.6 mL) was added to the flask under argon. The reaction medium was stirred at 30 °C for about 19 h with monomer conversion of *ca.* 27.2%, and a solution of TEMPO (0.154 g, 1 mmol) in 1 mL of degassed and anhydrous DMF was then added to quench the polymerization. The crude polymer solution was precipitated into a large excess (10 times) of cold diethyl ether. This purification step was repeated two times, and the obtained PVAc-*b*-PNVCL copolymer was dried under vacuum, chemical composition of $PVAc_{180}$-*b*-$PNVCL_{110}$ was confirmed by ^{1}H NMR spectroscopy analysis. ^{1}H NMR: (250 MHz, DMSO-d_6, 353 K, δ, ppm): 1.1–1.8 (–CH_2–CH– of VAc, –CH_2–CH– and –N–CH$_2$–CH_2–CH_2–CH_2–CH$_2$–CO– of NVCL), 1.8–2.0 (–OCOCH_3– of VAc), 2.2 (–N–CH$_2$–CH$_2$–CH$_2$–CH$_2$–CH_2–CO– of NVCL), 3.1 (–OC–N–CH_2– of NVCL), 4.1–4.5 (–CH$_2$–CH– of NVCL) and 4.7–4.9 (–CH$_2$–CH– of VAc) (see the ESI, Fig. S1a†). M_n of 5.67×10^4 g mol^{-1} and M_w/M_n of 1.06 were determined by SEC analysis in DMF with polystyrene as the calibration standard (see the ESI, Fig. S1c†).

To prepare the PVOH-*b*-PNVCL copolymer, a solution of $PVAc_{180}$-*b*-$PNVCL_{110}$ (4 g) in methanol (150 mL) was mixed with a solution of potassium hydroxide (1.75 g) in methanol (50 mL) in a 200 mL round-bottom flask. After stirring at room temperature for 15 h, the polymer solution was condensed to *ca.* 20 mL under reduced pressure. After dilution with de-ionized water, the mixture was dialyzed against de-ionized water (cut-off: 1000 Da) for another 48 h. The aqueous polymer solution was freeze-dried and a solid $PVOH_{180}$-*b*-$PNVCL_{110}$ polymer sample was obtained. ^{1}H NMR: (250 MHz, DMSO-d_6, 353 K, δ, ppm): 1.1–1.8 (–CH_2–CH– of VOH, –CH_2–CH– and –N–CH$_2$–CH_2–CH_2–CH_2–CH$_2$–CO– of NVCL), 1.9 (–OCOCH_3– of VOH), 2.2 (–N–CH$_2$–CH$_2$–CH$_2$–CH$_2$–CH$_2$–CH_2–CO– of NVCL), 3.1 (–OC–N–CH_2– of NVCL), 3.8–4.0 (–CH$_2$–CH– of VOH), 4.1–4.5 (–CH$_2$–CH– of NVCL and –OH of VOH) (see the ESI, Fig. S1b†).

LCST of 41 °C was confirmed for the $PVOH_{180}$-*b*-$PNVCL_{110}$ polymer solution (0.05 wt%, 1 °C min^{-1}) from turbidimetry measurement, and LCST was taken as the temperature at which transmittance at 700 nm started to decrease (PVOH-*b*-PNVCL in the following context refers to the $PVOH_{180}$-*b*-$PNVCL_{110}$ copolymer).

Preparation of maghemite nanoparticles (γ-Fe_2O_3 NPs). γ-Fe_2O_3 NPs were prepared *via* Massart's method.[46] 3.5 L of the iron(III) precursor ($FeCl_3 \cdot 6H_2O$, 0.32 mol) and iron(II) precursor ($FeCl_2 \cdot 4H_2O$, 0.16 mol) in de-ionized water were co-precipitated with 300 mL of ammonia hydroxide solution ($NH_3 \cdot H_2O$, 8.6 M) at room temperature. The solution turned black immediately, suggesting the formation of magnetite (Fe_3O_4) nanoparticles. After 15 min, the nanoparticles were collected with a permanent neodymium magnet, and the supernatant was discarded. Then the nanoparticles were suspended in 400 mL of nitric acid solution (2 M) under stirring for another 15 min. After collection of the nanoparticles and removal of the supernatant, 600 mL of ferric nitrate solution (0.33 M) were added and stirred at 90 °C for 30 min in order to oxidize magnetite into maghemite (γ-Fe_2O_3) nanoparticles. The maghemite nanoparticles were peptized with 400 mL of nitric acid (2 M) for 15 min. After rinsing with acetone (200 mL) 5 times, they were dispersed in 500 mL of de-ionized water. The final pH value of the final γ-Fe_2O_3 NPs suspension was tuned to 4.0, and the concentration to 61.5 g L^{-1}.

Surface functionalization of the γ-Fe_2O_3 NPs with 3-carboxy-5-nitrophenylboronic acid (CNPBA) (γ-Fe_2O_3–CNPBA). γ-Fe_2O_3–CNPBA NPs were prepared *via* a two-step procedure, as shown in Scheme 1-1. First, the γ-Fe_2O_3–APTES NPs were obtained from the condensation of (3-aminopropyl)-trimethoxysilane (APTES, 100 μL, 0.4 mmol) onto the surface of γ-Fe_2O_3 NPs (50 mg) in ethanol (50 mL) at 60 °C overnight. Then, the γ-Fe_2O_3–CNPBA NPs were obtained *via* the base-catalyzed amidation between the γ-Fe_2O_3–APTES NPs (25 mg) and CNPBA molecules (9 mg, 0.4 mmol) in anhydrous THF (50 mL) with DMAP (2 mg, 16 μmol) as the catalyst at room temperature for 48 h. For each step, the as-prepared nanoparticles were purified by three centrifugation/rinsing cycles (8000 rpm, 10 min), and then dried overnight under vacuum at 30 °C. The grafting concentration for APTES and CNPBA was estimated to be 0.40 and 0.25 molecule per nm^2, respectively, from TGA measurement (see the ESI, Fig. S2b†).

Reversibly crosslinked (RCL) PVOH-*b*-PNVCL nanogels. PVOH-*b*-PNVCL RCL nanogels were obtained after cooling down the RCL micelle solution, which was prepared above the LCST of the PNVCL block. Typically, the PVOH-*b*-PNVCL copolymer was dissolved in 20 mL of de-ionized water to obtain a polymer concentration of 0.05 wt% (7.8×10^{-5} mol VOH monomer units). The solution was then heated up to 50 °C under stirring, and immediately, a milky-white colloidal dispersion was observed, indicating the formation of thermo-induced micelles. After equilibration at 50 °C for another 20 min, 150 μL of the γ-Fe_2O_3–CNPBA NP suspension in THF (10 g L^{-1}) were added and the mixture was stirred under air for another 2 h, at the end of which the organic solvent (THF) was supposed to be fully evaporated. Then, after stirring overnight under airtight conditions, the RCL micelle solution was cooled down to room temperature and crude RCL nanogel dispersion was obtained (see the ESI, Fig. S3a†). After two-day dialysis (cut-off: 2000 Da)

against de-ionized water and subsequent freeze-drying, a light yellow powder was obtained.

Stability of the RCL nanogels. Stability studies of the RCL nanogels under acidic conditions or presence of glucose were carried out by monitoring the change in size under different pH values (7.4, 6.0 or 5.0) or glucose concentrations (0 or 100 mM). NaOH (0.1 M) and HCl (0.1 M) solutions were used to tune the pH value of the RCL nanogel dispersion, and dynamic light scattering (DLS) was utilized to follow the change in the hydrodynamic diameter (D_h) and size polydispersity (PDI).

Drug loading capacity and triggered release behaviours. Nile red (NR) was used as a drug model to test the drug loading capacity of the RCL nanogels, and a fluorometer was used to monitor the stimuli-triggered release under different conditions. Herein, after the thermal-induced formation of PVOH-*b*-PNVCL micelles at 50 °C (above the LCST), 2 mL of NR solution in THF (0.2 mg mL^{-1}) was added, then the mixture was stirred for 2 h in the dark to evaporate THF, while NR was supposed to migrate into the hydrophobic PNVCL domain. Then γ-Fe_2O_3–CNPBA NPs were added, following the same procedure. After removal of non-encapsulated NR *via* two-day dialysis and filtration, a pink dispersion was finally obtained (see the ESI, Fig. S3b†). Tamoxifen-loaded RCL nanogels were also prepared *via* the same protocol.

To estimate the drug loading capacity and efficiency, 0.1 mL of NR-loaded RCL nanogel dispersion was added to 5 mL of THF, in order to extract the NR fraction. The amount of NR was determined from its UV absorbance at 542 nm, thanks to a predetermined calibration curve. Drug loading capacity (DLC) and drug loading efficiency (DLE) were estimated according to the following formula:

$$\mathrm{DLC}\% = \frac{\text{mass of NR loaded}}{\text{mass of RCL nanogels}} \times 100\%$$

$$\mathrm{DLE}\% = \frac{\text{mass of NR loaded}}{\text{mass of NR fed}} \times 100\%$$

To study the release profile, 10 mL of the NR-loaded RCL nanogel dispersion (0.05 wt%) were sealed in a dialysis membrane (MWCO of 3500 Da), and then dialyzed against 100 mL of PBS (pH of 7.4, 6.0 or 5.0) buffer solutions with different glucose concentrations (5, 20 or 100 mM) under gentle stirring at 37 °C. The release behaviour in PBS buffer solution (no glucose, pH of 7.4) was taken as a blank. At each predetermined interval, 0.2 mL of the supernatant nanogel dispersion was drawn from the dialysis bag (released NR precipitated into the bottom of the dialysis bag) for fluorescence measurement, in order to estimate the retained NR amount. Fluorescence intensity was measured with a LS-55 Perkin Elmer fluorometer (Ex: 485 nm, Em: 590 nm) at 37 °C, and cumulative release was calculated according to this formula:

$$R = \frac{I_0 - I_t}{I_0} \times 100\%$$

where I_0 denotes the fluorescence intensity of NR-loaded RCL nanogel dispersion (0.05 wt%) before release, while I_t the fluorescence intensity of supernatant nanogel dispersion at a specific sampling time during the release experiments. All these values were obtained by deducting the fluorescence intensity of the blank RCL nanogel dispersion (without NR loading), to exclude the interference of fluorescence from the polymer and maghemite moieties, if any.

Cell culture and cytotoxicity of the RCL nanogels. The fibroblast-like L929 cell line was obtained from ATT (ATCC CCL-1) and grown at 37 °C under humidified air (5 vol.% of CO_2) in Dulbecco's modified eagle medium (DMEM, 4.5 g L^{-1} of glucose), which was supplemented with 5 vol.% of fetal bovine serum (FBS), 1 vol.% of glutamax, 1 vol.% of penicillin/streptomycin (10 000 units of penicillin (base) and 10 000 units of streptomycin (base) per mL) (DMEM complete medium). The human melanoma MEL-5 cells (originated from a non pigmented clone 32, gift from Dr G. Degiovanni, University of Liège) were cultured in DMEM complete medium. After rinsing with PBS (Ca^{2+}/Mg^{2+} free), the cells were detached with trypsin–EDTA (0.05–0.02 vol.%)/PBS (Ca^{2+}/Mg^{2+} free).

Cytotoxicity measurement was carried out with both L929 and MEL-5 cell lines. The L929 or MEL-5 cells were first seeded in a 96-well plate at a density of 5×10^3 cells per well and grown in 200 μL of DMEM complete medium for 24 h. After removal of the culture medium, the cells were then treated with 200 μL of RCL nanogels in DMEM complete medium at different concentrations (20, 50, 100 and 200 μg mL^{-1}) for 24 and 48 h, respectively. For each concentration, 5 parallel samples were carried out at the same time (technical replicates). After each incubation period, cells were rinsed with PBS (with Ca^{2+}/Mg^{2+}) and the cell viability was evaluated *via* the MTS assay. 20 μL of MTS and 100 μL of PBS (with Ca^{2+}/Mg^{2+}) were added, and then the plates were incubated for another 30 min at 37 °C. The absorbance at 490 nm was measured using a Power wave X (Biotek instrument Inc.) micro-plate reader. Percentages of cell viability were determined relative to untreated cells (control, 100% viability).

Studies on cellular uptake of the RCL nanogels within MEL-5 cells *via* fluorescence microscopy analysis. MEL-5 cells (3.8×10^5) were seeded in a 12-well plate in 2 mL of DMEM complete medium. After 24 h, the medium was replaced with 2 mL of NR-loaded RCL nanogel dispersion (20, 50, 100 and 200 μg mL^{-1}) in DMEM complete medium or fresh complete medium (control). After incubating for a predetermined period (3, 6, 15 or 24 h), the solution was removed and the cells were rinsed twice with PBS (with Ca^{2+}/Mg^{2+}) solution to eliminate the free nanogels. The cells were then treated with paraformaldehyde (4 vol.%)/DAPI (1 vol.%)/PBS(with Ca^{2+}/Mg^{2+}) at room temperature for another fifteen minutes in the dark. After rinsing with PBS (with Ca^{2+}/Mg^{2+}) twice, 2 mL of PBS (with Ca^{2+}/Mg^{2+}) were added. Analysis of the treated cells was performed with an Olympus IX81inverted fluorescence microscope.

Studies on cellular uptake of the RCL nanogels by MEL-5 cells *via* TEM observation. MEL-5 cells internalized with the RLC nanogels were also obtained by the previously described protocol. After the cells were detached with EDTA (0.2 vol.%)/PBS (Ca^{2+}/Mg^{2+} free), centrifuged (200*g*, 5 min), and re-dispersed in fresh PBS (Ca^{2+}/Mg^{2+} free), the cell pellet was fixed

with glutaraldehyde (4 wt%)/PBS (Ca^{2+}/Mg^{2+} free). After 24 h, the pellet was rinsed with PBS again (Ca^{2+}/Mg^{2+} free) to remove the free fixatives and then dehydrated in an alcohol series, embedded in Epon, and sliced for TEM observation with the Philips CM-100 microscope.

Studies on cellular uptake of the RCL nanogels within MEL-5 cells *via* cytofluorometry analysis. MEL-5 cells with internalized RCL nanogels were obtained *via* the previously described protocol. After removing the free nanogels, the cells were detached with trypsin–EDTA (0.05–0.02 vol.%)/PBS (Ca^{2+}/Mg^{2+} free), centrifuged (200*g*, 5 min), and re-dispersed in fresh PBS (with Ca^{2+}/Mg^{2+}). The treated MEL-5 cells were analyzed with a FACScan fluorescence-activated cell sorter (FACScan I, Becton-Dickinson). 400 μL of treated MEL-5 cells in PBS (with Ca^{2+}/Mg^{2+}) were used for this measurement, while untreated MEL-5 cells were taken as a blank. The fluorescence intensity and the percentage of cell-associated fluorescence were determined using CellQuest software. The ratio of the fluorescence intensity of 10 000 treated cells to that of 10 000 untreated cells was expressed as mean fluorescence intensity (MFI), which was employed to quantitatively evaluate the cellular uptake amount. The bar graphs in the figures represent mean value ±standard deviation from three independent replicates.

***In vitro* triggered release of tamoxifen (TAM) and cell recovery capability.** The cytotoxicity assessment of Tamoxifen (TAM) against the MEL-5 cells was also carried out according to the same protocol. Due to its hydrophobic property, TAM was first dissolved in DMSO at different concentrations, and then diluted by 1000 times with DMEM complete medium to obtain final DMSO concentration of 0.1 vol.%, and TAM concentrations of 1, 10, 20 and 50 μM. Then cytotoxicity potential of TAM was tested (see the ESI, Fig. S8a†) *via* the MTS assay, while cytotoxicity of DMEM complete medium supplemented with 0.1 vol.% DMSO was also tested for comparison.

The *in vitro* triggered release of TAM from the TAM-loaded RCL nanogels was followed within the MEL-5 cell culture, and the release amount was assessed *via* the variation in cell viability. Specifically, MEL-5 cells were treated with the TAM-loaded RCL nanogels (67 μg mL^{-1}) in DMEM complete medium with different pH values (7.4 or 5.0) and different glucose concentrations (5, 20 or 100 mM) for different incubation periods (3, 6, 12 or 24 h). Cell viabilities in DMEM complete medium without TAM-loaded RCL nanogels, but with a pH value of 7.4 or 5.0 and different glucose concentrations (5, 20 or 100 mM) for different periods (3, 6, 12 or 24 h) were also tested for comparison (see the ESI, Fig. S8b and S9†).

The cell recovery capability of the MEL-5 cells after the treatment was also evaluated *via* the MTS assay. After treatment with TAM-loaded RCL nanogels (67 μg mL^{-1}) in DMEM complete medium with different pH values (7.4 or 5.0) and different glucose concentrations (5, 20 or 100 mM) for 0.5 or 1 h, the cells were rinsed with PBS (with Ca^{2+}/Mg^{2+}) for two times to eliminate the free nanogels, and then incubated in fresh DMEM complete medium (pH 7.4) for another 24 h (doubling time for MEL-5 cells proliferation). Cell viabilities were checked *via* the same protocol, and cells without any treatment were taken as a control.

Statistical analysis. Cell culture experiments were performed on biological triplicates. Results are presented as mean value ±standard deviation. Statistical analyses of the data were performed using the unpaired and two-tailed Student's *t*-test. Statistical significance was determined at $P < 0.05$.

2.3 Characterization

Dynamic light scattering (DLS). Dynamic light scattering (DLS) measurements were carried out with a Malvern Instruments Nano-ZS system, which was equipped with a He–Ne laser (λ = 663 nm) and scattering angle of 90°. The correlation function was analyzed *via* the CONTIN method, and standard deviation was used to evaluate the size distribution (PDI). Every measurement was carried out with an RCL nanogel concentration of 0.05 wt%.

Fluorescence spectra. Fluorescence spectra of the NR-loaded RCL nanogel dispersion was recorded at room temperature using a LS-55 Perkin Elmer fluorometer, and fluorescence intensity (Ex: 485 nm, Em: 590 nm) was averaged from three independent measurements. For each measurement, the RCL nanogel concentration was fixed at 0.05 wt%.

Thermogravimetry analysis (TGA). Thermogravimetry analysis (TGA) of the surface-functionalized γ-Fe_2O_3 NPs or RCL nanogels was performed by heating to 100 °C at 50 °C min^{-1} and equilibrating for 10 min, and then the TGA curves were recorded upon heating to 500 °C at 20 °C min^{-1} in air with a TA Q500 Instrument.

Magnetization measurements. Magnetization measurements of the RCL nanogels and bare γ-Fe_2O_3 NPs were conducted with a 5MPMS superconducting quantum interference device (SQUID) in the field range from −6000 to 6000 Oe at 300 K.

AMF-induced heating experiments. AMF-induced heating experiments were performed at 755 kHz, and 14 mT in a field coil (35 mm × 4 turns). An eppendorf tube containing 1.5 mL of the RCL nanogel aqueous suspension with a known concentration was placed in the centre of the coils, and then the heating process was monitored with a fibre optical sensor to trace the change in temperature.

Proton relaxometry measurement. Proton relaxometry measurement of the RCL nanogels was performed with a Stelar Fast Field-Cycling Spectrometer FFC-2000 equipped with a permanent magnet for the relaxation measurements in the range of 0.01–40 MHz at 37 °C. Additional data were obtained at 60 MHz on a minispec mq-60 (Bruker) analyzer.

3. Results and discussion

3.1 Preparation of PVOH-*b*-PNVCL RCL nanogels

The general strategy for the synthesis of the thermo-, pH- and glucose-responsive nanogels is summarized in Scheme 1. First, a well-defined double-hydrophilic poly(vinyl alcohol)-*b*-poly(*N*-vinylcaprolactam) (PVOH-*b*-PNVCL) copolymer was prepared *via* the cobalt-mediated radical polymerization (CMRP) technique[42,43,47] following our previously reported procedure.[44] (see the ESI, Fig. S1†) Second, the self-assembly of the

PVOH-*b*-PNVCL copolymer into micelles was promoted by increasing the temperature from 25 to 50 °C, thus above the LCST of the PNVCL block (41 °C). The hydrophobic core is formed by the dehydrated PNVCL block while the corona consists of the hydrophilic PVOH block. Then, boronic acid-bearing γ-Fe_2O_3 NPs were used as crosslinking agents for the PVOH corona at 50 °C *via* the well-established boronate/diol bonding. Finally, the targeted RCL nanogels, integrating thermo-, glucose-, pH- and magnetism-responsiveness into one nano-object, were obtained after cooling down below the LCST of the PNVCL block (Scheme 1–2).

In order to introduce boronic acid groups onto the surface of 7.5 nm maghemite nanoparticles (γ-Fe_2O_3–CNPBA NPs), a two-step surface modification process was carried out. Briefly, (3-aminopropyl)triethoxysilane (APTES) molecules were first immobilized onto the surface of the γ-Fe_2O_3 NPs *via* a condensation reaction to introduce amine groups (γ-Fe_2O_3–APTES NPs), then 3-carboxy-5-nitrophenylboronic acid molecules (CNPBA) were grafted *via* amidation reaction onto the amino-functionalized nanoparticles, as shown in Scheme 1-1. The success of surface modification was evidenced by FTIR analysis (Fig. 1a). Indeed, the spectrum of γ-Fe_2O_3–APTES NPs exhibits a band at 1150 cm^{-1} with a shoulder at 1050 cm^{-1} typical to antisymmetric Si–O–Si vibrations resulting from the condensation of silanol groups to form a thin polysiloxane film over the γ-Fe_2O_3 NPs. On the other hand, two broad bands at 3419 and 1628 cm^{-1} can be ascribed to the N–H stretching and bending vibrations, respectively. After the amidation reaction between γ-Fe_2O_3–APTES NPs and the CNPBA molecules, new peaks at 2950, 1376, 1576 and also 1736 cm^{-1}, associated with the =C–H vibrations of the phenyl ring, C–B vibration, phenyl ring vibrations and C=O stretching, respectively, proved the presence of CNPBA molecules on the surface of γ-Fe_2O_3 NPs. The surface modification was also confirmed by XPS analysis of the γ-Fe_2O_3–CNPBA NPs (see the ESI, Fig. S2a†), with the signal at 192 eV, which is attributed to the B 1s peak. The TEM image of the γ-Fe_2O_3–CNPBA NPs (Fig. 1b) showed nearly the same size as bare γ-Fe_2O_3 NPs due to the low electronic density of the surface organic layer. Stepwise surface modification of the γ-Fe_2O_3 NPs was further quantitatively analyzed by thermogravimetric analysis (TGA, see the ESI, Fig. S2b†). On the basis of the weight fraction assigned to the organic components, the surface coverage of APTES in the γ-Fe_2O_3–APTES NPs (as a grafting density) was estimated to be *ca.* 0.40 molecule per nm^2, suggesting a medium surface coverage, compared to 4.5 molecules per nm^2 reported before,[48] due to a lower feeding amount of APTES. In addition, the grafting density of CNPBA molecules was estimated to be *ca.* 0.25 molecule per nm^2, namely, *ca.* 44 boronic acid groups per γ-Fe_2O_3 NP, by taking the average diameter of 7.5 nm into consideration.

The as-formed γ-Fe_2O_3–CNPBA NPs were then used to crosslink the thermo-induced PVOH-*b*-PNVCL micelles above the LCST, as described in Scheme 1-2. A light-yellow stable suspension of the RCL nanogels was obtained (see the ESI, Fig. S3a†). The slight coloration is due to the presence of γ-Fe_2O_3 NPs. The TEM image of the RCL nanogels is shown in Fig. 2a, and spherical RCL nanogels are observed, with an average size of *ca.* 80 nm confirmed. Presence of the γ-Fe_2O_3 NPs could be clearly seen in the partially-magnified TEM image (Fig. 2a-inset). The spherical morphology and size of the RCL

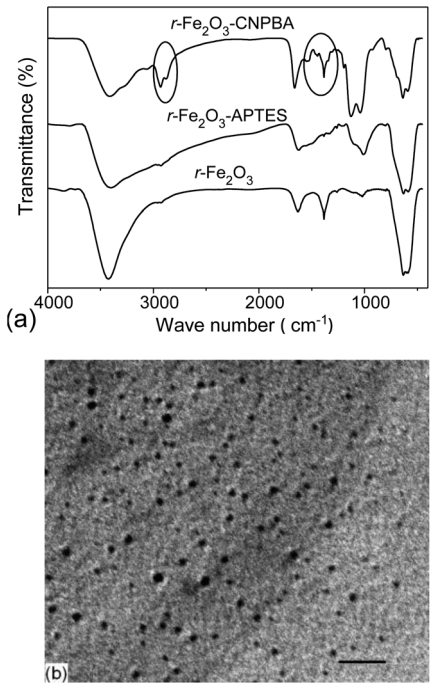

Fig. 1 FTIR spectra (a) and TEM image (b) of the γ-Fe_2O_3–CNPBA NPs (scale bar: 50 nm).

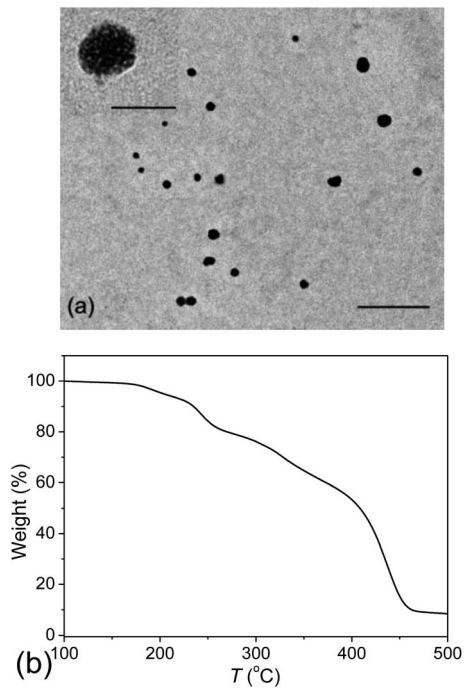

Fig. 2 Representative TEM image of the RCL nanogels (scale bar: 500 nm), and inset: partially-magnified TEM image of one nanogel particle (scale bar: 100 nm) (a), and TGA trace of the RCL nanogels from 100 to 500 °C (b).

nanogels were also confirmed by SEM observation (see the ESI, Fig. S4a and S4b†). The D_h of the RCL nanogels was confirmed to be *ca.* 530 nm (PDI 0.19) from DLS analysis (see the ESI, Fig. S4c†). The large deviation of size between TEM and DLS is attributed to the hydrated and swollen state of DLS samples, and the dehydrated and collapsed state of TEM samples. A γ-Fe_2O_3 content of *ca.* 10 wt% was confirmed by TGA measurement (Fig. 2b).

3.2 Stability of PVOH-*b*-PNVCL RCL nanogels

For those different vehicles aimed for DDS application, taking polymer micelles as an example, superior physical stability is a fundamental requirement, to make sure that they could withstand dissociation and premature cargo release during the delivery. On the other hand, they should dissociate upon exposure to some stimuli after targeting to a desirable site, so that triggered release could be accomplished. Thus, it becomes necessary to study the stability of the RCL nanogels under different conditions before exploring the DDS applications. As reported in some previous literature,[7,44,47] PNVCL-based copolymers exhibited sharp responsiveness to temperature, and the size of the physically-assembled micelles gradually increased upon increase in temperature due to the inter-micelle agglomeration. Here, thermo-responsiveness and stability of the RCL nanogels were also studied under different temperatures by DLS, and evolution of D_h and PDI is summarized in Fig. 3. As shown, in contrast to those physically-assembled micelles, the size of the RCL nanogels sharply decreased from *ca.* 530 to 300 nm (slight change in PDI) within a narrow temperature range. This de-swelling behaviour could be attributed to the thermo-induced dehydration of the PNVCL block, and a phase transition temperature was detected at *ca.* 40 °C, near the LCST of 41 °C. Moreover, unlike those non-crosslinked micelles in our previous reports,[44,47] no inter-micelle agglomeration occurred during the heating process, thanks to the shell-crosslinking.

In an aqueous solution of boronate derivatives, obvious pH responsiveness could be observed,[24] due to the equilibrium between the protonated and de-protonated states of the boronate functionality. The reversible nature of the boronate/diol bonding originates from the formation of cyclic boronate esters with 1,2- or 1,3-diols, which effectively lowers the pK_a of the boronic acid groups.[15] Therefore, it is anticipated that these boronate/diol crosslinked nanogels could dissociate into unimers upon exposure to a low pH value (below the pK_a) or competing low-molecular-weight diols, for example, glucose. Stability of the RCL nanogels under acidic pH (5.0) or presence of glucose (100 mM) was also studied. RCL nanogels at a pH of 7.4 without glucose were taken as the blank, and size distribution patterns of the RCL nanogels after each treatment are all summarized in Fig. 3b. As shown, in the blank sample (pH 7.4, no glucose), the size distribution slightly changed, suggesting stable crosslinked nanostructures. However, after 6 h treatment with glucose (100 mM, pH 7.4), the D_h of the RCL nanogels decreases sharply to 130 nm, approaching the D_h of the γ-Fe_2O_3–CNPBA NPs (100 nm). This deviation might be attributed to the attaching of glucose molecules onto the γ-Fe_2O_3–CNPBA NPs and/or remaining few PVOH-*b*-PNVCL macromolecular chains on the surface of γ-Fe_2O_3 NPs. Furthermore, a new peak in the range of 1–10 nm is observed, attributed to the free PVOH-*b*-PNVCL polymer chains after nanogel dissociation. RCL nanogels after glucose treatment were also analyzed by TEM (see the ESI, Fig. S5a†), no crosslinked nanogels could be detected anymore, but only small nanoparticles (<10 nm), similar to the γ-Fe_2O_3–CNPBA NPs in Fig. 1b.

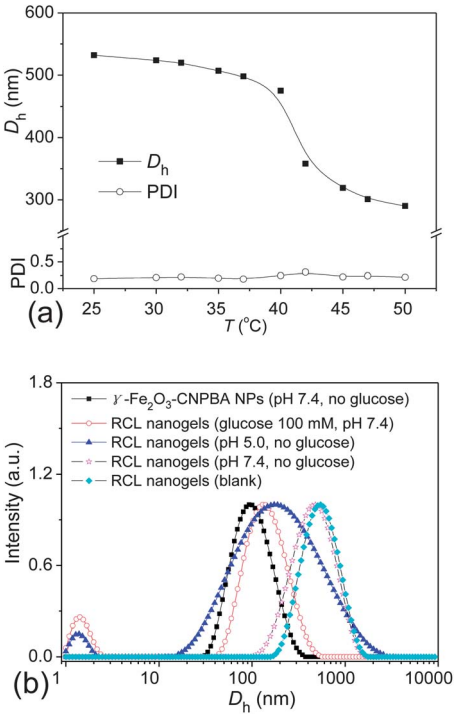

Fig. 3 Evolution of hydrodynamic diameter (D_h) and size distribution (PDI) of the RCL nanogels under a gradual heating process (a); intensity-averaged size distribution of the RCL nanogels after 6 h treatment (37 °C) of glucose (100 mM, pH 7.4), acidic pH (pH 5.0, no glucose) and physiological pH (pH 7.4, no glucose), as well as the γ-Fe_2O_3–CNPBA NP aqueous suspension (pH 7.4, no glucose) and the as-prepared RCL nanogels (pH 7.4, no glucose) (intensities of all the size distribution traces were normalized and concentrations of all the nanogels were fixed at 0.05 wt%), (b).

Stability of the RCL nanogels under an acidic condition (pH 5.0) was also investigated, in light of pH-dependence of the boronate/diol bonding. As shown in Fig. 3b, the D_h of the RCL nanogels decreased to 190 nm upon 6 h treatment under pH of 5.0. On the other hand, a new peak originating from those free macromolecular chains is also observed. Compared to the size distribution of the RCL nanogels treated with glucose (100 mM, pH 7.4), a much broader distribution is observed for the nanogels under acidic condition (pH 5.0, 0 mM glucose). TEM analysis evidences the presence of free γ-Fe_2O_3 NPs, but in the form of aggregates (see the ESI, Fig. S5b†), due to the hydrophobic property of the boronic acid groups below its pK_a. These results demonstrate that the RCL nanogels are stable enough under physiological pH (7.4) in the absence of glucose; whereas, they would readily dissociate into unimers upon exposure to acidic pH (below pK_a) or/and to low-molecular-weight diols,

such as glucose. Therefore, potential pH- and glucose-triggered drug release could be envisaged, once these RCL nanogels are developed as DDS.

3.3 Magnetic properties of PVOH-*b*-PNVCL RCL nanogels

Due to the presence of the γ-Fe_2O_3 NPs in the crosslinked shell, the RCL nanogels are also expected to exhibit some specific magnetic properties. The magnetization curve was first recorded with a SQUID apparatus at 300 K and is illustrated in Fig. 4a. The zero hysteresis of the *M–H* curve at zero magnetic field indicates the superparamagnetic properties of the RCL nanogels (Fig. 4a-i), similar to that of the γ-Fe_2O_3–CNPBA NPs (Fig. 4a-ii). The magnetization (*M*) at 6000 Oe decreases from *ca.* 55.2 emu (per g γ-Fe_2O_3–CNPBA NPs) to 5.1 emu (per g nanogels). The extremely low *M* value for nanogels is easily explained by the high content of the non-magnetic polymer component (*ca.* 90 wt% from TGA measurements, Fig. 2b). By taking into account this content, *M* at 6000 Oe was estimated to be *ca.* 51.0 emu per (g γ-Fe_2O_3–CNPBA NPs), similar to the value of the bare γ-Fe_2O_3–CNPBA NPs.

In light of the superparamagnetic properties of the RCL nanogels, local heating could be expected upon exposure to external alternating magnetic field (AMF). To explore the possibility of AMF-induced heating, RCL nanogel aqueous suspensions with different concentrations were placed in an AMF (755 kHz, 14 mT). A 37 °C water bath was introduced to mimic the physiological temperature, and variation in temperature was recorded with an optical thermo-sensor and is summarized in Fig. 4b. It could be seen that the RCL nanogel dispersions were heated up by extending the duration of AMF treatment. Moreover, higher temperatures were reached with higher concentrations, while negligible heating up of *ca.* 0.1 °C was detected for the Milli-Q water (as a blank). Specific loss power (SLP), which is defined as the power generated per unit mass of the sample (W g^{-1}), was calculated according to the following formula:

$$\mathrm{SLP} = \frac{c_\mathrm{p}}{m_{\mathrm{Fe_2O_3}}} \times \frac{\mathrm{d}T}{\mathrm{d}t}$$

where c_p is the specific heat capacity of the suspension (4.186 J ($g^{-1}\cdot K^{-1}$)), d*T*/d*t* is the initial slope of the temperature *vs.* time (K s^{-1}) when AMF was applied, *m* is the mass of the γ-Fe_2O_3–CNPBA NPs inside the RCL nanogels. A SLP value was estimated to be 20.6 W g^{-1}, comparable to the value of 26.1 W g^{-1} in our previous system of γ-Fe_2O_3 NPs coated with poly(acrylic acid)-*b*-poly(vinyl alcohol).[3] Moreover, due to the heating-capacity of the RCL nanogel dispersion, it is envisaged that conformational change of the nanogels might occur during the AMF application. Thus, the AMF treatment might also post an effect on the subsequent release behaviours, which will be explored in the following section.

Magnetic nanoparticles have been of great interest as MRI contrast agents in the past few decades owing to their high contrast resolution. To further demonstrate the versatility of these RCL nanogels, the MRI contrast enhancement performance was also investigated. Nuclear magnetic relaxation dispersion (NMRD) profiles, displaying the evolution of proton longitudinal relaxivity in the applied magnetic field, were recorded with the RCL nanogels. The r_1-NMRD profiles (Fig. 4c) were characterized by the presence of a low-field plateau, a peak at about 4 MHz for γ-Fe_2O_3 NPs and 3 MHz for the RCL nanogels, respectively, and a final decrease to zero at a higher Larmor frequency. The peak is caused by the successive alignment of magnetic moments, which is induced by the increased magnetic field, indicating a typically superparamagnetic relaxation profile. To better understand the relaxivity, the NMRD profiles were fitted according to the SPM theory developed by Muller and his co-workers.[49] Fitting of the r_1-NMRD profiles could provide us the following parameters: saturation magnetization (M_s), radius of the crystal (R_NMR) and Néel relaxation time ($\tau_\mathrm{Néel}$), the values of which are all listed in the legend of Fig. 4c. As compared, decrease in M_s might result from the presence of the organic component, while increase in R_NMR and shifting of the peak to lower field might be due to the clustering of γ-Fe_2O_3 NPs within the RCL nanogels, as shown in the TEM image (Fig. 2a). The cluster structure, however, did not significantly affect $\tau_\mathrm{Néel}$. In order to demonstrate the potential application of these RCL nanogels as MRI contrast agents, we collected the MRI images at 7 T on a Bruker Biopsec 70/16 scanner. As shown in Fig. 4d, difference in the brightness could be clearly observed at an echo time of 164.7 ms between the RCL nanogels (right side, [Fe] = 0.16 mM) and the blank of PVOH-*b*-PNVCL aqueous solution (left side, 0.5 g L^{-1}), showing a significant negative contrast enhancement (signal darkening). Moreover, this might also suggest the possibility of tracing the RCL nanogels during the delivery, with the help of MR imaging.

3.4 Drug loading capability and triggered release behaviours of PVOH-*b*-PNVCL RCL nanogels

Most of the orally delivered drugs (40–50%), either synthetic or herbal, present poor water solubility and they might suffer from inadequate bioavailability and lack of dose proportionality after administration.[14] Therefore, the improvement of drug solubility remains one of the most challenging aspects of pharmacy research and development, especially for those oral DDS. There are numerous vehicles available and reported in the scientific literature, such as surfactants, liposomes, polymer micelles, *etc.*,[13–16] which could effectively improve the solubility of those poorly water-soluble chemotherapeutic agents. These vehicles usually provide a hydrophobic reservoir, in which the hydrophobic drugs can be easily encapsulated. In this study, Nile Red (NR) was chosen as a hydrophobic model drug with very poor water solubility (<1 μg mL^{-1} at 25 °C). Our encapsulation strategy is based on the thermal-induced micellization of PVOH-*b*-PNVCL above the LCST (Scheme 1-2), in which hydrophobic NR molecules could be accommodated within the hydrophobic PNVCL domain. After shell-crosslinking with γ-Fe_2O_3–CNPBA NPs, the system was cooled down below the LCST, and NR was successfully loaded within the RCL nanogels (un-encapsulated NR was removed *via* filtration). As shown in Fig. S3b,† a stable and light pink dispersion of NR-loaded RCL nanogels was clearly observed, indicating the successful loading

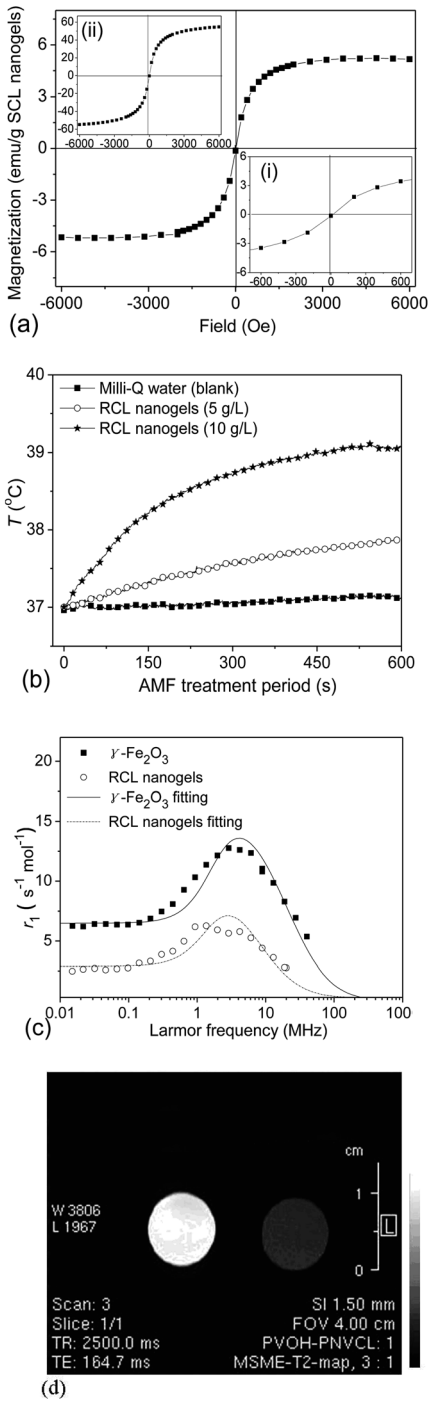

Fig. 4 Magnetization curves of the RCL nanogels, inset-(i): partially amplified curve of the RCL nanogels in the range of −620 to 620 Oe and inset-(ii): magnetization curve of the bare γ-Fe_2O_3–CNPBA NPs (a); AFM-induced heating profiles of the RCL nanogel aqueous solutions (10 and 5 g L^{-1}) under alternating magnetic field (AMF, 755 kHz, 14 mT), and pure Milli-Q water was taken as a blank (b); nuclear magnetic resonance dispersion (NMRD) profiles of the RCL nanogels and bare γ-Fe_2O_3 NPs, parameters obtained from the SPM theory fitting for the RCL nanogels: $\tau_{Néel} = 4.8$ ns, $M_s = 3.5$ A m^2 kg^{-1}, $D_{NMR} = 15$ nm; while for the bare γ-Fe_2O_3 NPs: $\tau_{Néel} = 4.0$ ns, $M_s = 21.7$ A m^2 kg^{-1}, $D_{NMR} = 8.0$ nm (c); T_2-weighted MR images of the RCL nanogel aqueous suspension (right side, [Fe] = 0.16 mM) and PVOH-*b*-PNVCL copolymer aqueous solution (left side, 0.5 g L^{-1}) at 164.7 ms (d).

of hydrophobic NR. Furthermore, presence of NR inside the RCL nanogels was also confirmed by the specific UV/vis absorption at *ca.* 600 nm (see the ESI, Fig. S3c†). Moreover, the drug loading capacity (DLC) of *ca.* 10 wt% and drug loading efficiency (DLE) of *ca.* 24% were confirmed *via* the procedure described in the experimental part.

As discussed in the section of stability of the RCL nanogels, they are stable enough under physiological pH (7.4) in the absence of glucose, while lowering the pH below the pK_a of CNPBA or adding competing low-molecular-weight diols leads to the dissociation of crosslinked nanostructures. Thus, it is expected that triggered release of the loaded cargos could also be accomplished upon lowering pH and/or adding competing low-molecular-weight diols, such as glucose. The release behaviours of the NR-loaded RCL nanogels under different conditions were followed with a fluorometer, and the release profiles are presented as cumulative release in Fig. 5. As shown in Fig. 5a and b negligible release was observed when there was neither glucose nor variation in pH (7.4), while less than 10% of NR was released in 24 h at a pH of 7.4 and glucose concentration of 5 mM, the same glucose concentration in the Dulbecco's modified eagle medium (DMEM) complete medium for MEL-5 cell culture and also the same as the normal blood sugar level. As reported previously,[22,27,50] an acidic condition (below the pK_a) might facilitate the cleavage of the boronate/diol bonding, resulting in dissociation of crosslinked structures and subsequent cargo release, despite of various glucose concentrations. Similar to those reports, pH-dependent release behaviours are also observed with the NR-loaded RCL nanogels. For instance, at a fixed glucose concentration of 5 mM (Fig. 5b), decrease in pH from 7.4 to 5.0 resulted in the increase in release from 10% to 43% after 24 h. It deserves to be noted that these acidic conditions were a simulated environment of early endosomes and late endosomes (lysosomes). Moreover, it is reported that nano-scale DDS could be taken up by the cells *via* the endocytosis process,[51,52] which starts at physiological pH of 7.4, drops to a lower pH of 5.9–6.2 in early endosomes and finally approaches a pH of 4.5–5.0 in late endosomes (lysosomes).[53] Therefore, it might be envisaged that the change of pH during the endocytosis process could also contribute to dissociation of nanogels and the subsequent release.

Moreover, addition of glucose leads to new bonding between boronate groups and glucose molecules, consequently inducing the dissociation of RCL nanogels into PVOH-*b*-PNVCL unimers. This cascade of events could also contribute to the cargo release. Here, at a specific pH, for example pH of 6.0, matching the pK_a of CNPBA, when the glucose concentration increased from 0 to 100 mM, the drug release rate increases significantly, from 6% (0 mM, Fig. 5a) to 65% (100 mM, Fig. 5d) in 24 h. Moreover, we can also highlight the synergistic contribution of lowering pH and adding some glucose on the drug release behaviours. For example, we could observe a release of 71% under pH 5.0 and 20 mM glucose (Fig. 5c), compared to 5% under pH 7.4 and 0 mM glucose (Fig. 5a) after 24 h. These results all support the controlled release behaviours through the variation in pH or/and glucose concentration in the biologically-relevant release environment.

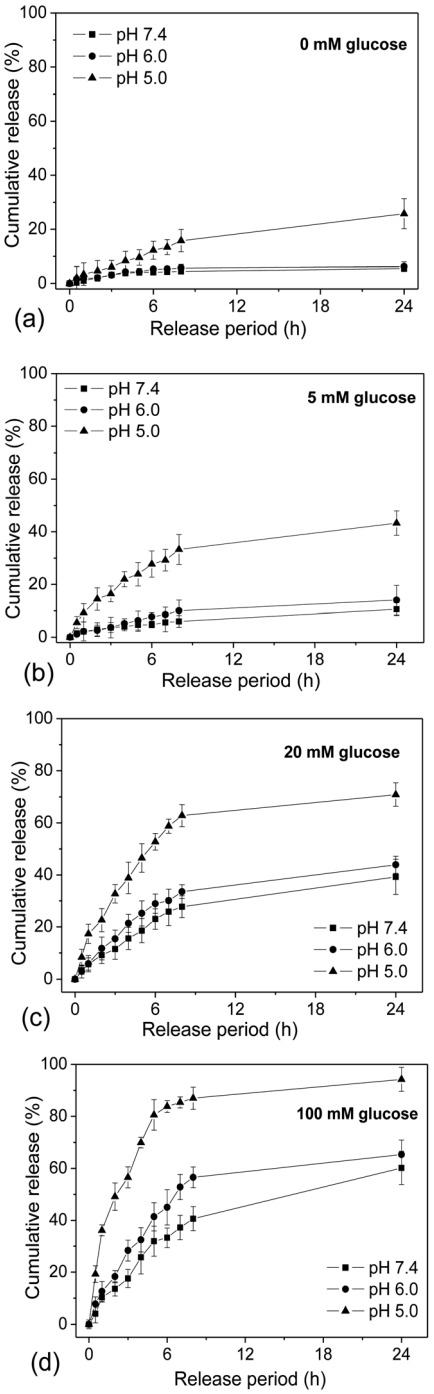

Fig. 5 Triggered drug release profiles of NR from the NR-loaded RCL nanogels at glucose concentrations of 0 mM (a), 5 mM (b), 20 mM (c) and 100 mM (d) under different pH values at 37 °C, respectively.

For those glucose-triggered DDS, it might be a contradictory concept for DDS which are expected to release the cargoes under higher glucose concentration, for example 20 mM blood sugar for diabetes, but also accomplish a minimal release before targeting the desirable disease sites, since blood sugar concentration might be of the same level in the whole vascular system. Fortunately, as far as we know, the blood sugar concentration is highly dependent on the biological rhythms, for example different blood sugar concentrations before and after taking meals, huge differences between day and night, *etc.* Thus, introduction of this kind of drug-loaded RCL nanogels could be performed at lower glucose concentrations, accompanied with blood sugar concentration monitoring. On the other hand, the following increase in glucose concentration might be in favour of triggering the release, in order to achieve a higher therapeutic efficiency. Moreover, it could be also used in combination with some other therapies, for example, Glucophage®, which is a commercially available product to control the blood sugar concentration. Of course, this research is a proof-of-concept work on these pH- and glucose-responsive RCL as DDS. Further examination and optimization should be done before their *in vivo* use for diabetic treatment, bio-sensing, *etc.*

As discussed above, local heating can be generated upon exposure of the RCL nanogel suspension to external AMF. This AMF application is therefore expected to affect the release profiles. Herein, the release behaviours were recorded at pH 7.4 and 37 °C with different glucose concentrations. Fig. 6a evidences that application of AMF accelerates the NR release for each glucose concentration. Evolution of the temperature of the release medium was also recorded during this AMF treatment, and a maximum temperature of *ca.* 37.5 °C was observed in Fig. 6b. This mild heating up of the surrounding medium could avoid damage to the healthy tissues. On the other hand, since the local temperature was indeed much higher than that of the release medium,[54,55] the accelerated release could be explained

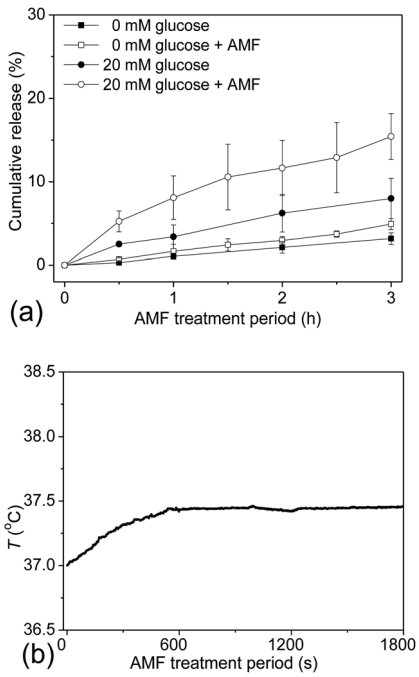

Fig. 6 Triggered release profiles of NR from the NR-loaded RCL nanogel aqueous solution (5 g L^{-1}) with different glucose concentrations (0 and 20 mM) at pH value of 7.4 and 37 °C with or without AMF treatment (a), and evolution of the temperature of the release medium during the AMF-triggered release in the first 30 min treatment (b).

by the higher local heating, that further contributes to an increased diffusion coefficient. It deserves to note that there is a very slight increase in NR release under AMF and 0 mM glucose compared to that under 20 mM glucose. This difference might be explained by the presence of crosslinking and the highly hydrophobic property of NR. In light of the loading strategy, NR molecules were mainly accumulated within the inner PNVCL domain, rather than the external PVOH shell. Thus, without de-crosslinking, mild heating of the systems might not be able to contribute to the release of those hydrophobic cargoes, unlike hydrophilic cargoes. Based on the AMF-induced release behaviours, we might emphasize the supplementary, rather than the dominant, contribution of the external AMF application. So the AMF-triggered release is an extensional application for the presence of superparamagnetic nanoparticles. On the other hand, we might emphasize more on the potential role, as MRI contrast agents or *in vivo* tracking components, of these nano-vehicles. Faster release of chemotherapeutic agents is known to lead to better bioavailability and a higher apoptosis rate.[14] Thus, remote AMF application might also be useful to improve the efficiency of therapeutic treatment, with a higher spatial and temporal control.

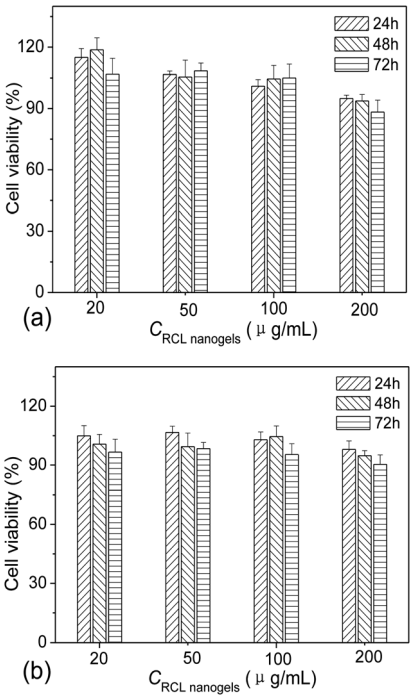

Fig. 7 Cytotoxicity profiles of the RCL nanogels against mouse fibroblast-like L929 cell line (a) and human melanoma MEL-5 cell line (b) under different concentrations after 24, 48 and 72 h incubation in DMEM complete medium (5 mM glucose); percentage viabilities were expressed relative to the un-treated cells (control, 100% viability). Results are all presented as mean value ±standard deviation ($n = 5$).

3.5 Cytotoxicity and cellular uptake of PVOH-*b*-PNVCL RCL nanogels

Although the approach to multifunctional crosslinked micelles/nanogels presents numerous opportunities in biomedical applications, such as potential DDS, there are still some concerns on the safety of these materials following human exposure. Cytotoxicity evaluation has become a commonly-used method in toxicology to assess the biocompatibility of a material designed for biomedical applications. Studies on the cytotoxicity of these RCL nanogels against mouse fibroblast-like L929 cell line (Fig. 7a) and human melanoma MEL-5 cell line (Fig. 7b) were carried out in DMEM complete medium (5 mM glucose) *via* the MTS assay. Data showed negligible cytotoxicity of the RCL nanogels in the concentration range of 1–200 μg mL^{-1} in comparison with the control, with low proliferation inhibitive effect (*ca.* 10%), even under higher concentrations (200 μg mL^{-1}) and longer incubation (72 h). These results suggest that these RCL nanogels present good biocompatibility in the concentration range of 1–200 μg mL^{-1}.

Surface functionality is one of the most important factors that might decide the *in vivo* fate of nano-sized DDS. It is reported that the PEG- or PVOH-based surfaces can effectively increase the biocompatibility, optimize the long-term colloidal stability[56] and also inhibit the uptake by macrophages *via* MPS[57] and/or renal clearance process.[58] Thus, the PVOH-based corona and stable crosslinking nanostructures (under physiological pH) of these RCL nanogels might ensure a longer circulation half-time.

Fluorescence microscope was first used to characterize the cellular uptake behaviour and qualitatively study the intracellular distribution of the RCL nanogels. Due to the accessible fluorescent luminance of NR (Ex: 485 nm, Em: 590 nm), this hydrophobic model drug can be also used as a fluorescence probe to visualize the RCL nanogels. Typical fluorescence microscopy image of the treated MEL-5 cells are shown in Fig. 8a, after 12 h incubation with the NR-loaded RCL nanogels (100 mg L^{-1}). Red fluorescence (nanogels, Nile red) could be observed inside the cells around the blue fluorescence (nuclei, DAPI) in the overlapped image in Fig. 8a-4, indicating a preferential accumulation within the cytoplasm. Due to the limitation of the fluorescence microscope in discerning individual nano-vehicles after internalization, the treated MEL-5 cells were fixed and then sliced for TEM observation. Fig. 8b shows the typical TEM image of the treated MEL-5 cells, and in the partially-amplified image, we could find some individual γ-Fe_2O_3 NPs (marked with arrows) within some vehicles, which might be endosomes or endolysosomes. This finding corroborates the dissociation of RCL nanogels into unimers and individual γ-Fe_2O_3 NPs under acidic pH during the endocytosis process and/or presence of glucose (5 mM), in agreement with the result on stability of the RCL nanogels (Fig. 3b and Fig. S5†)

Fluorescence-activated cell sorting (FACS) measurement was also carried out to study the auto-fluorescence of those treated cells and confirm the cellular uptake of the NR-loaded RCL nanogels within the MEL-5 cells, even though most of them were disintegrated within the cellular compartments. Cyto-fluorometric histogram of the NR fluorescence, originating from the RCL nanogels, was shown in Fig. S6,† with untreated cells as a control. The cytofluorometric analysis clearly confirmed the internalization of the RCL nanogels with the

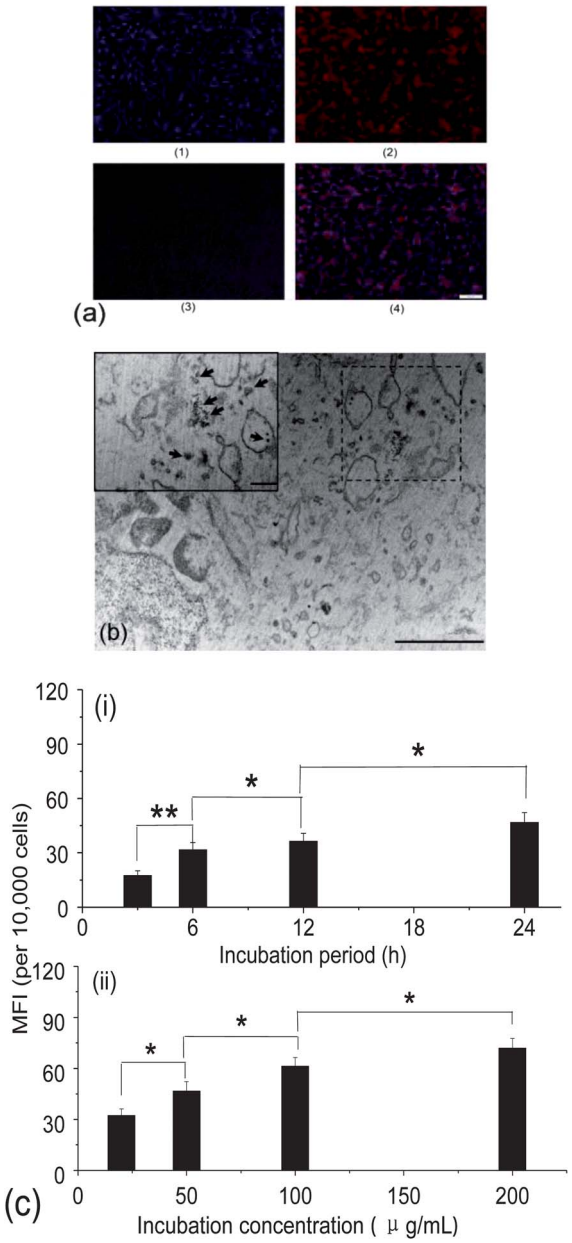

Fig. 8 Fluorescence microscopy image of the MEL-5 cells after 12 h incubation with the NR-loaded RCL nanogels (100 μg mL^{-1}): cellular nuclei stained with DAPI (a-1, blue), fluorescence pattern of NR (a-2, red), phase contrast pattern (a-3), emerged image (a-4, scale bar: 100 μm); TEM image of the treated MEL-5 cells after 12 h incubation with the RCL nanogels (100 μg mL^{-1}) in DMEM complete medium with 5 mM glucose (scale bar: 2 μm), insert: partially-magnified image of the area marked with dotted rectangle (scale bar: 200 nm, b); and dependence of mean fluorescence intensity (MFI) of the treated MEL-5 cells on incubation period (c-i, 100 mg L^{-1}) as well as incubation concentration (c-ii, 12 h) after incubation with NR-loaded RCL nanogels, (* = $P < 0.05$, ** = $P < 0.01$ by the Students' t-test, $n = 3$).

distinct shift of the fluorescence distribution peak. Additionally, nearly 100% of the cells were internalized with the NR-loaded RCL nanogels after 12 h incubation. Quantitative analysis of the cellular uptake amount was also conducted by cytofluorometric analysis. The ratio of fluorescence intensity per 10 000 treated cells to that of 10 000 untreated cells, expressed as mean fluorescence intensity (MFI), was taken as an indirect measurement to evaluate the cellular uptake efficiency. Herein, the dependence of MFI of the treated cells on the incubation period (fixed concentration of 100 μg mL^{-1}) as well as incubation concentration (fixed period of 12 h) is summarized in Fig. 8c. A fast increase in MFI is detected along with the extension of the incubation period, however, with slight increase after 12 h incubation (Fig. 8c-i). Additionally, a concentration-dependent internalization is also observed from the MFI when the cells were incubated with more RCL nanogels (Fig. 8c-ii).

3.6 *In vitro* triggered release of tamoxifen

Tamoxifen citrate (TAM), a BCS class II model drug, is an anticancer drug widely used for the treatment of early and advanced estrogen-dependent breast cancer in pre- and post-menopausal women.[59] TAM is slightly soluble in water (0.3 μg mL^{-1}), thus loading of TAM into the RCL nanogels could effectively improve its solubility and permeability, without changing its chemical structure. TAM-loaded RCL nanogels (RCL@TAM) were also prepared according to the procedure described in the experimental part and drug loading capacity (DLC) of 8.3 wt% and drug loading efficiency (DLE) of 32% were estimated with a pre-established calibration curve (see the ESI, Fig. S7†), in the same level with the DLC and DLE for NR.

In the preliminary studies, toxicity of TAM and RCL@TAM nanogels against MEL-5 cells was first tested. As shown in Fig. S8a,† the MEL-5 cells retained a high viability in the presence of DMSO (0.1 vol.%) or TAM (<1 μM) after 24 h incubation. However, cell viability decreased sharply when the TAM concentration exceeded 10 μM. The cytotoxicity of bare TAM was then compared with that of RCL@TAM nanogels. For this purpose, we fixed RCL@TAM nanogel concentration at 67 μg mL^{-1} (TAM of 10 μM), in order to match the toxic window of TAM and study the *in vitro* triggered release of TAM within the culture of MEL-5 cells. Cytotoxicity of the RCL@TAM nanogels (67 μg mL^{-1}) is summarized in Fig. 9a. As shown, at pH 7.4 and 5 mM glucose, the TAM@RCL nanogels exhibited less toxicity to MEL-5 cell line (*ca.* 90% viability after 24 h incubation) compared to bare TAM (*ca.* 21% viability after 24 h incubation, 10 μM). However, slight cell proliferation inhibition was observed (*ca.* 10%) compared to the control of the blank RCL nanogel vehicles (Fig. 7b, 50 μg mL^{-1}, without TAM loaded). The low cell-inhibiting effect might be attributed to the dominant location of those internalized nanogels within the early endosomes. Since pH of the endosome micro-environment is 5.9–6.2, it is not sufficient to dissociate all the reversibly crosslinked nanostructures, even if we can observe some maghemite nanoparticles in Fig. 8b. Or, the diffusion of the TAM molecules within the late endosomes (endolysosomes) might be restricted even if the nanogels are dissociated, thus higher cell viability was observed here. Anyway, the release of chemotherapeutic agents within endosomes and/or the hypothesis on restricted diffusion needs to be confirmed in our following work.

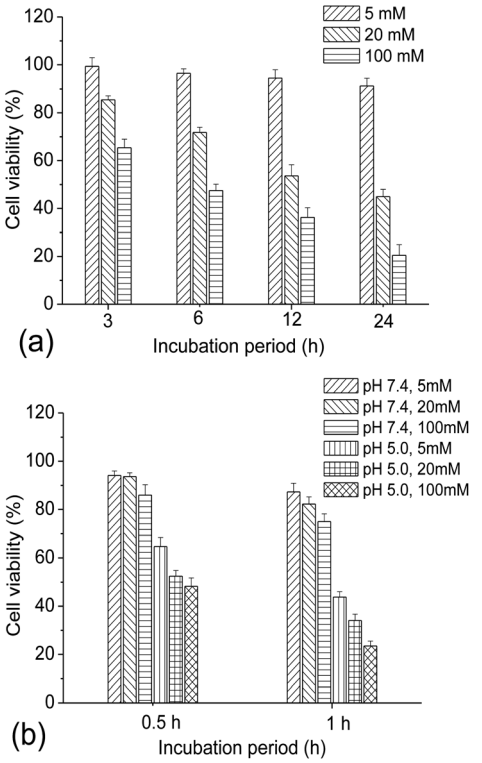

Fig. 9 Cell viability of MEL-5 cells against RCL@TAM nanogels (67 μg mL^{-1}, TAM 10 mM) at pH 7.4 with different glucose concentrations after 24 h incubation (a); and cell viability of MEL-5 cells against RCL@TAM nanogels (67 μg mL^{-1}, TAM 10 mM) at pH 7.4 or 5.0 with different glucose concentrations after 0.5 h or 1 h incubation (b). Percentage viabilities were expressed relative to the un-treated cells (control, 100% viability), and results were all presented as mean value ±standard deviation ($n = 5$).

To investigate the triggered release under acidic pH (5.0) or/and higher glucose concentrations (20 mM or 100 mM), controls were first tested by estimating the cell viability under these conditions without TAM@RCL nanogels. The accelerated cell proliferation was confirmed by more glucose present in the culture medium at a pH of 7.4 (see the ESI, Fig. S8b†), due to the increased ATP production rate under high glucose concentration. Under acidic conditions, for example pH of 5.0, it is reported that the cell proliferation was significantly inhibited.[60] However, part of the cell viability could be maintained under acidic pH in the presence of more glucose, since the high amount of ATP produced for the F_0F_1-ATPase is in favour of expelling H^+ ions out of the cells.[61] In Fig. S9a,† the cell viability after 3 h incubation under pH of 5.0 was also presented. As expected, the cells suffered from a significant loss in viability within few hours, compared with the same treatment at pH of 7.4 (see the ESI, Fig. S9b†). On the other hand, relatively higher cell viability was observed when more glucose was present at pH of 5.0.

Then, the studies on *in vitro* cytotoxicity of the TAM@RCL nanogels at pH of 7.4 (physiological pH) with different glucose concentrations were carried out and results are summarized in Fig. 9a. It was found that the TAM@RCL nanogels showed significantly enhanced inhibition on cell proliferation, especially with higher glucose concentration, compared to the control of RCL nanogels (Fig. 7b). This could be attributed to the faster release of TAM in the intracellular compartments, caused by the dissociation of the RCL nanogels *via* glucose competitive replacement. Additionally, the cell-proliferation inhibition by the TAM@RCL nanogels also shows a positive dependence on the incubation period, due to the sustainable release of the TAM.

MEL-5 cell viabilities were also studied after exposure to TAM@RCL nanogels under pH 5.0 (lysosome pH) with different glucose concentrations (Fig. 9b). Short exposure periods, 0.5 h and 1 h incubation were used to test the triggered release behaviour, in order to avoid the high-level cytotoxicity caused by the acidic pH. Compared with the viability at pH of 7.4 after 0.5 or 1 h incubation, significant growth inhibition of the MEL-5 cells was observed at pH of 5.0, due to both TAM and acidic pH. Moreover, compared with the cell viability under pH of 5.0 without TAM@RCL nanogels (see the ESI, Fig. S9a†), a further decrease in cell viability was observed, which could be assigned to the activation of released TAM.

Primary therapeutic mechanism of tamoxifen involves the competitive binding to estrogen receptors on tumour cells or other tissue targets, producing a nuclear complex that decreases DNA synthesis, inhibiting estrogen effects and arresting the cell cycle.[59,62] Cell survival capability, namely the retention of proliferative or metabolic activities of treated cells compared to the untreated controls, provides evaluation over the sensitivity of cells to various treatments in the long term.[63] Usually, this assay is used to better understand the biological importance of some proteins or pathways which leads to an observed phenotype after exposure to cytotoxic agents.[64] Here, we also tested the cell recovery capability of the treated MEL-5 cells. After 0.5 h and 1 h incubation with the RCL@TAM nanogels at pH of 7.4 or 5.0 (viability shown in Fig. 9b), the free nanogels were removed and the treated cells were allowed to recover in fresh DMEM complete medium (pH 7.4, 5 mM glucose) and subsequently

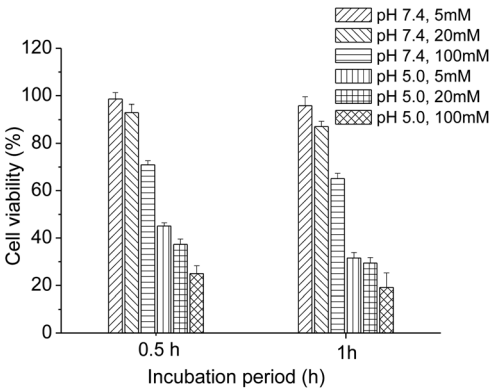

Fig. 10 Cell survival capability of MEL-5 cells after incubation with RCL@TAM nanogels (67 μg mL^{-1}, TAM 10 mM) at pH 7.4 or 5.0 with different glucose concentrations after 0.5 h and 1 h, and afterwards a further 24 h incubation in fresh DMEM medium (pH 7.4, 5 mM glucose). Percentage viabilities were expressed relative to the un-treated cells (control at pH 7.4 and 5 mM glucose, 100% viability), and results were all presented as mean value ±standard deviation ($n = 5$).

respond *via* proliferation, if they can, for another 24 h (doubling time of MEL-5 cells). The cell viabilities are summarized in Fig. 10. It is observed that the treated cells recover viability much easier when previously incubated at a pH of 7.4 with lower glucose concentration, compared to the acidic pH 5.0 with higher glucose concentration, since less TAM molecules interact with the MEL-5 cells. For those treated cells previously incubated under pH of 5.0, the cell viability remained at the same level, even a little bit lower than that before recovery. Taking into consideration that the number of control cells doubled during the post-incubation process, we can also deduce that a part of the treated cells also recovered during this period.

4. Conclusions

In summary, we developed stimuli-responsive reversibly cross-linked (RCL) nanogels based on poly(vinyl alcohol)-*b*-poly(*N*-vinylcaprolactam) (PVOH-*b*-PNVCL) copolymers and boronic acid-functionalized γ-Fe_2O_3 NPs, *via* the boronate/diol bonding above the LCST of the PNVCL block. Hydrophobic drugs could be easily loaded (DLC of *ca.* 10 wt%) and well trapped within the resulting RCL nanogels under pH of 7.4. Upon decrease in pH (5.0) or presence of glucose (5–100 mM), triggered release of the drug payloads could be accomplished, as a result of the cleavage of boronate/diol bonding. Due to the superparamagnetic properties of the γ-Fe_2O_3 NPs as well as RCL nanogels, concentration- and period-dependent AMF-induced heating could be generated under alternating magnetic field (AMF, 755 kHz, 14 mT) application. Accordingly, AMF application was also implemented to accelerate the drug release, with a mild heating of the surrounding. Moreover, enhanced T_2-weighted MRI contrast performance was also evidenced. Cytotoxicity of the RCL nanogels against L929 and MEL-5 lines revealed a good biocompatibility of these RCL nanogels for biomedical application. Possibilities of pH- and/or glucose-triggered *in vitro* release of the pre-loaded tamoxifen were confirmed with the enhanced inhibition of cell-proliferation in DMEM complete medium with an acidic pH (5.0) and/or presence of glucose (5, 20 or 100 mM). This multi-functional DDS, combined with potential stimuli-triggered release and MRI enhancement, could be developed as a general platform for theranostic applications.

Acknowledgements

The authors thank the Belgian National Funds for Scientific Research (F.R.S.-FNRS), the European Community in the frame of the Erasmus Mundus International doctoral school IDS-FunMat and the Science Policy Office of the Belgian Federal Government (PAI VII-05) for their financial support. The authors are grateful to Prof. Sébastien Lecommandoux and Dr Olivia Sandre for the access to the magnetic hyperthermia setup at Laboratoire de Chimie des Polymères Organiques, University of Bordeaux. The authors also thank Dr Christine Labrugère (ICMCB/CECAMA) for XPS analyses, and also GIGA-imaging and the flow cytometry platform in the University of Liège. C.D. is the Research Director and A.D. is a Research Associate by the F.R.S.-FNRS, Belgium. L.V.E and S.L. would like to thank the FNRS, ARC, the Science Policy Office of the Belgian Federal Government (PAI VII-11) and ENCITE programs for financial support.

Notes and references

1 J. Gao, H. Gu and B. Xu, *Acc. Chem. Res.*, 2009, **42**, 1097–1107.
2 S. Ganta, H. Devalapally, A. Shahiwala and M. Amiji, *J Control Release*, 2008, **126**, 187–204.
3 J. Liu, C. Detrembleur, A. Debuigne, M. C. De Pauw-Gillet, S. Mornet, L. Vander Elst, S. Laurent, C. Labrugere, C. Jerome and E. Duguet, *Nanoscale*, 2013, **5**, 11464–11477.
4 S. Cajot, K. Van Butsele, A. Paillard, C. Passirani, E. Garcion, J. P. Benoit, S. K. Varshney and C. Jerome, *Acta Biomater*, 2012, **8**, 4215–4223.
5 J. Liu, C. Detrembleur, A. Debuigne, M. C. De Pauw-Gillet, S. Mornet, L. Vander Elst, S. Laurent, C. Jerome and E. Duguet, *J. Mater. Chem. B*, 2014, **2**, 59–70.
6 S. Louguet, B. Rousseau, R. Epherre, N. Guidolin, G. Goglio, S. Mornet, E. Duguet, S. Lecommandoux and C. Schatz, *Polym. Chem.*, 2012, **3**, 1408–1417.
7 J. Liu, C. Detrembleur, M. Hurtgen, A. Debuigne, M. C. De Pauw-Gillet, S. Mornet, E. Duguet and C. Jerome, *Polym. Chem.*, 2014, **5**, 77–88.
8 S. Cajot, N. Lautram, C. Passirani and C. Jerome, *J Control Release*, 2011, **152**, 30–36.
9 Y. Li, W. Xiao, K. Xiao, L. Berti, J. Luo, H. P. Tseng, G. Fung and K. S. Lam, *Angew Chem Int Ed*, 2012, **51**, 2864–2869.
10 C. R. Gordijo, K. Koulajian, A. J. Shuhendler, L. D. Bonifacio, H. Y. Huang, S. Chiang, G. A. Ozin, A. Giacca and X. Y. Wu, *Adv. Funct. Mater.*, 2011, **21**, 73–82.
11 J. Liu, C. Detrembleur, M. C. De Pauw-Gillet, S. Mornet, E. Duguet and C. Jerome, *Polym. Chem.*, 2014, DOI: 10.1039/c1033py01057k, in press.
12 J. Liu, C. Detrembleur, B. Grignard, M. C. De Pauw-Gillet, S. Mornet, E. Duguet and C. Jerome, *Chem. - Asian J.*, 2014, **9**, 275–288.
13 D. Schmaljohann, *Adv Drug Deliv Rev*, 2006, **58**, 1655–1670.
14 K. Kataoka, A. Harada and Y. Nagasaki, *Adv Drug Deliver Rev*, 2001, **47**, 113–131.
15 D. Roy, J. N. Cambre and B. S. Sumerlin, *Prog. Polym. Sci.*, 2010, **35**, 278–301.
16 H. A. Klok, A. Rosler and G. W. M. Vandermeulen, *Adv Drug Deliver Rev*, 2001, **53**, 95–108.
17 R. K. O'Reilly, C. J. Hawker and K. L. Wooley, *Chem. Soc. Rev.*, 2006, **35**, 1068–1083.
18 S. Y. Liu, X. Z. Jiang and R. Narain, *Langmuir*, 2009, **25**, 13344–13350.
19 K. Wang, G. Luo, Y. Liu, L. Cao, S. X. Cheng, R. X. Zhuo and X. Z. Zhang, *Polym. Chem.*, 2012, **3**, 1084–1090.
20 J. F. Gohy and Y. Zhao, *Chem. Soc. Rev.*, 2013, **42**, 7117–7129.
21 D. Han, X. Tong and Y. Zhao, *Langmuir*, 2012, **28**, 2327–2331.
22 D. Roy, J. N. Cambre and B. S. Sumerlin, *Chem. Commun.*, 2009, 2106–2108.
23 B. Wang, R. Ma, G. Liu, Y. Li, X. Liu, Y. An and L. Shi, *Langmuir*, 2009, **25**, 12522–12528.

24 J. Zou, S. Zhang, R. Shrestha, K. Seetho, C. L. Donley and K. L. Wooley, *Polym Chem*, 2012, **3**, 3146–3156.
25 G. Ye and X. Wang, *Biosens. Bioelectron.*, 2010, **26**, 772–777.
26 I. Tokarev and S. Minko, *Adv Mater*, 2010, **22**, 3446–3462.
27 M. Piest, X. Zhang, J. Trinidad and J. F. J. Engbersen, *Soft Matter*, 2010, **7**, 11111–11118.
28 A. P. Bapat, D. Roy, J. G. Ray, D. A. Savin and B. S. Sumerlin, *J. Am. Chem. Soc.*, 2011, **133**, 19832–19838.
29 Y. Zhao, B. G. Trewyn, I. I. Slowing and V. S. Lin, *J. Am. Chem. Soc.*, 2009, **131**, 8398–8400.
30 L. Sun, X. Zhang, C. Zheng, Z. Wu and C. Li, *J. Phys. Chem. B*, 2013, **117**, 3852–3860.
31 J. Tan, H. F. Wang and X. P. Yan, *Anal. Chem.*, 2009, **81**, 5273–5280.
32 T. Chen, D. P. Chang, T. Liu, R. Desikan, R. Datar, T. Thundat, R. Berger and S. Zauscher, *J. Mater. Chem.*, 2010, **20**, 3391–3395.
33 C. Cui, E. M. Bonder, Y. Qin and F. Jäkle, *J. Polym. Sci., Part A: Polym. Chem.*, 2010, **48**, 2438–2445.
34 Q. Jin, L. P. Lv and G. Y. Liu, *Polymer*, 2011, **51**, 3068–3080.
35 G. Bisker, D. Yeheskely-Hayon, L. Minai and D. Yelin, *J Control Release*, 2012, **162**, 303–309.
36 J. C. Cambre and B. S. Sumerlin, *Polymer*, 2011, **51**, 3068–3080.
37 W. Yang, J. Yan, H. Fang and B. Wang, *Chem. Commun.*, 2003, 792–793.
38 M. Lee, T. I. Kim, K. H. Kim, J. H. Kim, M. S. Choi, H. J. Choi and K. Koh, *Anal. Biochem.*, 2002, **310**, 163–170.
39 A. Matsumoto, R. Kurata, D. Shiino and K. Kataoka, *Macromolecules*, 2004, **37**, 1502–1510.
40 J. Yan, G. Springsteen, S. Deeter and B. Wang, *Tetrahedron*, 2004, **60**, 11205–11209.
41 H. R. Mulla, N. J. Agard and A. Basu, *Bioorg. Med. Chem. Lett.*, 2004, **14**, 25–27.
42 A. Debuigne, R. Poli, C. Jerome, R. Jerome and C. Detrembleur, *Prog. Polym. Sci.*, 2009, **34**, 211–239.
43 M. Hurtgen, C. Detrembleur, C. Jerome and A. Debuigne, *Polym. Rev.*, 2011, **51**, 886–894.
44 M. Hurtgen, J. Liu, A. Debuigne, C. Jerome and C. Detrembleur, *J. Polym. Sci., Part A: Polym. Chem.*, 2012, **50**, 400–408.
45 A. Debuigne, Y. Champouret, R. Jerome, R. Poli and C. Detrembleur, *Chem Eur J*, 2008, **14**, 4046–4059.
46 R. Massart, *IEEE Trans. Magn.*, 1981, **17**, 1247–1248.
47 A. Kermagoret, C. A. Fustin, M. Bourguignon, C. Detrembleur, C. Jerome and A. Debuigne, *Polym. Chem.*, 2013, **4**, 2575–2583.
48 S. Mornet, J. Portier and E. Duguet, *J. Magn. Magn. Mater.*, 2005, **293**, 127–134.
49 A. Roch, R. Muller and P. Gillis, *J. Chem. Phys.*, 1999, **110**, 5403–5411.
50 T. Levy, C. Dejugnat and G. B. Sukhorukov, *Adv. Funct. Mater.*, 2008, **18**, 1586–1594.
51 Q. He, Z. Zhang, F. Gao, Y. Li and J. Shi, *Small*, 2011, **7**, 271–280.
52 J. Panyam and V. Labhasetwar, *Adv Drug Deliv Rev*, 2003, **55**, 329–347.
53 D. R. Lynch and S. H. Snyder, *Annu. Rev. Biochem.*, 1986, **55**, 773–799.
54 E. Duguet, S. Vasseur, S. Mornet and J. M. Devoisselle, *Nanomedicine*, 2006, **1**, 157–168.
55 S. Mornet, S. Vasseur, F. Grasset, P. Veverka, G. Goglio, A. Demourgues, J. Portier, E. Pollert and E. Duguet, *Prog. Solid State Chem.*, 2006, **34**, 237–247.
56 M. J. Roberts, M. D. Bentley and J. M. Harris, *Adv Drug Deliv Rev*, 2002, **54**, 459–476.
57 J. Xie, C. Xu, N. Kohler, Y. Hou and S. Sun, *Adv. Mater.*, 2007, **19**, 3163–3166.
58 H. S. Choi, W. Liu, P. Misra, E. Tanaka, J. P. Zimmer, B. Itty Ipe, M. G. Bawendi and J. V. Frangioni, *Nat. Biotechnol.*, 2007, **25**, 1165–1170.
59 C. K. Osborne, *New Engl J Med*, 1998, **339**, 1609–1618.
60 R. C. Fitzgerald, M. B. Omary and G. Triadafilopoulos, *J. Cell Sci.*, 1997, **110**, 663–671.
61 B. M. Corcoran, C. Stanton, G. F. Fitzgerald and R. P. Ross, *Appl. Environ. Microbiol.*, 2005, **71**, 3060–3067.
62 S. J. Chatterjee and S. Pandey, *Cancer Biol Ther*, 2011, **11**, 216–228.
63 J. M. Dziba, R. Marcinek, G. Venkataraman, J. A. Robinson and K. B. Ain, *Thyroid*, 2002, **12**, 1063–1070.
64 A. Eulalio, I. Behm-Ansmant and E. Izaurralde, *Nat Revi Mol Cell Biol*, 2007, **8**, 9–22.